Heat Mass Transfer (2015) 51:941–952
DOI 10.1007/s00231-014-1466-2

ORIGINAL

Numerical sensitivity analysis of density driven CO_2 convection with respect to different modeling and boundary conditions

Sylvie Chevalier · Titly Farhana Faisal · Yves Bernabe · Ruben Juanes · Mohamed Sassi

Received: 6 April 2014 / Accepted: 23 November 2014 / Published online: 7 December 2014

Abstract We present a numerical analysis of the sensitivity of the density driven CO_2 convection results in a vertical Hele-Shaw cell with respect to different modeling assumptions. The role of density driven convection phenomenon in CO_2 geological storage capacity and safety has already been pointed out in several studies. We showed that in order to accurately simulate the phenomenon occurring in lab experiments, multi-phase transfer has to be considered and variations in the permeability field should also be taken into account. Taylor dispersion has been found to have no significant effect on the results. Experimental results of the convection fingering process development and of quantitative determination of the total mass of dissolved CO_2 were used to validate the numerical simulation results. Understanding how accurate numerical models can simulate lab experiments is an important step in confirming their reliability to predict underground CO_2 storage capacity.

List of symbols

b	Hele-Shaw cell aperture (m)
D	Diffusion coefficient (m^2/s)
D_{Tay}	Taylor dispersion coefficient (m^2/s)
g	Acceleration of gravity (m/s^2)
h	Diffusive layer thickness (m)
h_c	Pressure head difference between phases (m)
H	Hele-Shaw cell height (m)
$\mathbf{J}$	Diffusive flux (kg/m^3s)
$\mathbf{k}$	Intrinsic permeability (m^2)
k_r	Relative permeability (−)
m	Van Genuchten third parameter (−)
m_d	Mass rate density (kg/sm^3)
n	Van Genuchten second parameter (−)
M	Molecular weight (kg/kmol)
P	Pressure (Pa)
S	Saturation (−)
S_{el}	Effective water saturation (−)
S_r	Irreducible water saturation (−)
t	Time (s)
t_{conv}	Onset time of convection (s)
U	Average velocity in the flow direction (m/s)
$\mathbf{V}$	Advective flux (m/s)
W	Hele-Shaw cell width (m)
$\mathbf{z}$	Unit gravitation direction vector

Subscripts

atm	Atmospheric
l	Aqueous
g	Gas

Superscript

i	H_2O or CO_2

Greek symbols

α	Van Genuchten first parameter (−)
ϕ	Porosity (−)
γ	Phase index (liquid or gaseous)
ρ	Density (kg/m^3)
τ	Tortuosity (−)
μ	Viscosity (Pa s)
ω	Mass fraction (−)
χ	Mole fraction (−)

S. Chevalier · T. F. Faisal · M. Sassi (✉)
Masdar Institute of Science and Technology, P.O. Box 54224, Abu Dhabi, UAE
e-mail: msassi@masdar.ac.ae

Y. Bernabe · R. Juanes
Massachusetts Institute of Technology, 77 Massachusetts Avenue, Building 48, Cambridge, MA 02139, USA

1 Introduction

Geological CO_2 storage in deep saline aquifers is one of the most promising near-term solutions in mitigating anthropogenic atmospheric CO_2 emissions. However, the transfer phenomena related to the storage may occur over centuries. The decision to store CO_2 underground will be mainly based on numerical predictions. But predictions on reservoir time and space scales are difficult to validate because data are generally sparse and will only be useful for a small part of the relevant time period [1]. Therefore, the reliability of numerical models to reproduce physical results is an essential pre-requisite in order to trust numerical long-term predictions at large scale. Laboratory scale data are valuable to validate the numerical models. The numerical work reported in this paper is related to former experimental works [2–4]. In particular, we investigate the accuracy and relevance of critical assumptions used in modeling. Our objective is to gain a better understanding of the physical processes of CO_2 geological storage at the reservoir scale and so to enhance the degree of confidence in underground capacity storage predictions.

2 Background

In this paper, we consider density-driven convection of dissolved CO_2 in water, one of the phenomena thought to occur when CO_2 is stored in saline aquifers [2]. Several authors used stability analysis to investigate the conditions controlling the onset of convection and its development at large scales [1, 5–9]. Sensitivity of convection to Rayleigh number and media characteristics such as geometrical dimensions or anisotropy was of particular interest. Other authors used direct numerical simulation to investigate the long term behavior of the phenomenon. Pruess [10] used the numerical model TOUGH2/ECO2N [11] in order to simulate density driven convection and estimate the dissolution rates of CO_2 for different permeabilities of the porous medium. He concluded that the convection pattern was very sensitive to small changes in problem specifications but not the total CO_2 dissolution rate. Pau et al. [8] also found that, despite the chaotic nature of the convection process, basic measures such as onset time and CO_2 mass flux related to convective activity are robust and insensitive to limited variations of the problem inputs. Hidalgo and Carrera [12] included CO_2 dispersion in the simulation and showed that it can reduce the onset time of convection by up to two orders of magnitude. Farajzadeh et al. [13, 14] and Ranganathan et al. [15] studied numerically density driven convection in a 2D configuration similar to Hele-Shaw cell. They identified three regimes depending on the heterogeneity characteristics of the permeability fields and they noted that the CO_2 dissolution rate is larger in heterogeneous media than in a homogeneous one.

Few studies presented direct comparison of experimental results to numerical simulations. Namely laboratory tests in transparent Hele-Shaw cells were performed by Kneafsey and Pruess [2, 3] and compared to numerical simulations. They obtained reasonable agreement except for noticeably different timescales. However, they did not present any experimental data of total dissolved CO_2 mass in the Hele-Shaw cells.

The numerical simulations presented in this paper use experimental results of CO_2 density driven convection mass transfer experiments in Hele-Shaw cells for comparison and validation [4]. In particular, we attempted to compare results in terms of convection patterns, timescales and total dissolved CO_2 mass. We analyzed the effects of the top boundary condition (water and CO_2 gas interface), Taylor dispersion and cell gap non-uniformity on the agreement between numerical and experimental results. We demonstrated that at this scale and conditions (1) the multiphase transfer between water and CO_2 gas cannot be ignored, (2) Taylor dispersion is a non-significant parameter for the mass transfer in Hele-Shaw configuration and (3) permeability non-uniformities have a significant effect on the three parameters (convection pattern, timescale, and total CO_2 mass transfer).

3 Model formulation

3.1 Physical model

The physical model used in our simulations reproduced the experimental configuration. We considered a Hele-Shaw cell (height H = 22 cm and width W = 15 cm) with an aperture b equal to 1, 0.7, 0.5 and 0.3 mm (Fig. 1), filled with water and overlaid by CO_2 at room conditions of 22 °C and atmospheric pressure. The lateral and bottom sides of the cell were impervious.

In order to simulate the boundary conditions at the top of the cell, we considered two possibilities. Firstly, we did not include a separate CO_2 gas phase and only considered CO_2-saturated water interface (Fig. 1a). This assumption is the one used by [1, 10, 13–16]. In general, this assumption leads to underestimation of timescales and overestimation of total CO_2 mass transfer compared to experimental data. Secondly, we considered a multiphase problem, with the presence of a pure CO_2 gas layer in contact with water across a sharp interface, a more realistic representation of our Hele-Shaw cell (Fig. 1b). The presence of such a gas layer was simulated by Kneafsey and Pruess [2, 3] and produced an overestimation of numerical timescales in comparison with the experimental ones. Here, the results

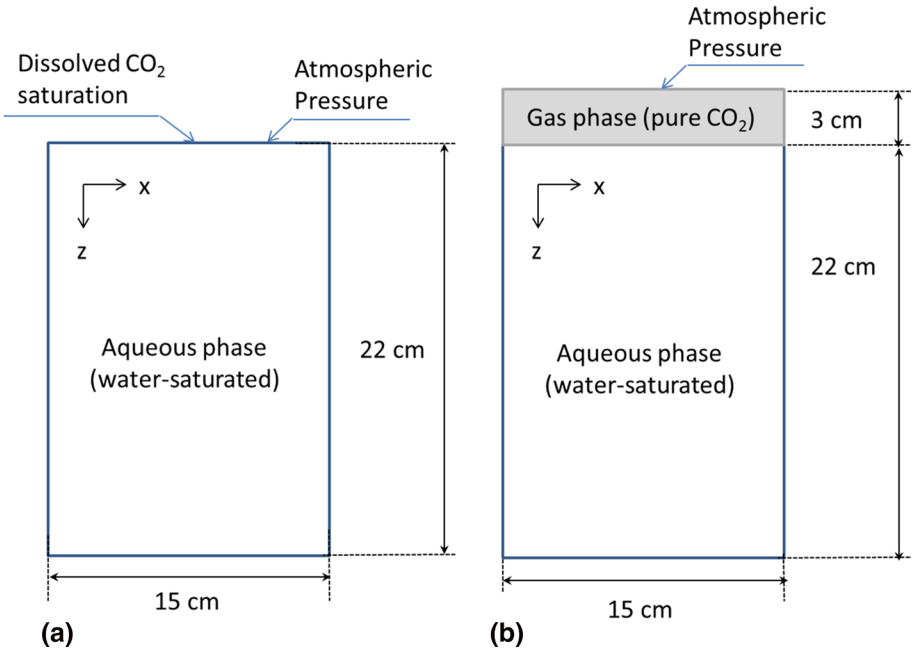

Fig. 1 Physical models **a** single phase condition and **b** two-phase condition

obtained with the second assumption (presence of gas) also overestimated the numerical timescale but were in better agreement for the total dissolved CO_2 mass results with the experimental results than the one obtained with the single phase assumption. To complete the study, we numerically analyzed the possible effect of Taylor dispersion and of variations of the cell aperture. Including permeability heterogeneity noticeably improved the agreement with all experimental results.

3.2 Numerical model

3.2.1 Governing equations

This work assumed that the convective motion in the Hele-Shaw cell is mathematically analogous to two-dimensional flow in a porous medium. This approach was used by Kneafsey and Pruess [2, 3] for similar conditions. The governing equations presented below are valid for both configurations of Fig. 1a, b. However for the first configuration, water and CO_2 exist only in aqueous phase. For the latter configuration, water and CO_2 are assumed to exist in aqueous (l) and gas (g) phases under equilibrium conditions. The global formulation for the conservation equations of water and CO_2 masses is:

$$\frac{\partial}{\partial t}\left[\sum_{\gamma=l,g}\left(\phi\rho_\gamma S_\gamma \omega_\gamma^i\right)\right] = -\sum_{\gamma=l,g}\nabla\left(\rho_\gamma \omega_\gamma^i \mathbf{V}_\gamma\right) - \sum_{\gamma=l,g}\nabla\left(\mathbf{J}_\gamma^i\right) + \sum_{\gamma=l,g}\left(\omega_\gamma^i m_{d\gamma}\right) \quad (1)$$

where γ indicates the phase (gas or liquid), i represents the species (H_2O or CO_2); ϕ (−) the porosity, ρ (kg/m^3) the density, S (−) the saturation, ω (−) the mass fraction, m_d (kg/sm^3) the mass rate density.

The left term in Eq. 1 represents the change in the conserved quantity within a volume over time. The two first right terms represent the net flux of the conserved quantity into the volume (advective and diffusive fluxes) and the last one represents any net source of the conserved quantity within the volume.

Darcy's law is used to compute the advective fluxes V_γ (m/s) of the mobile phases (for $\gamma = l, g$):

$$\mathbf{V}_\gamma = -\frac{k_{r\gamma}\mathbf{k}}{\mu_\gamma}\left(\nabla P_\gamma + \rho_\gamma g\mathbf{z}\right) \quad (2)$$

where k_r is relative permeability, $\mathbf{k}$ intrinsic permeability (m^2), μ (Pa s) viscosity, P (Pa) pressure, g (m/s^2) acceleration of gravity and $\mathbf{z}$ unit gravitation direction vector.

In the diffusive flux computations [$\mathbf{J}$ (kg/m^{3}s)], molecular diffusion is considered but mechanical dispersion is neglected (for $\gamma = l, g$):

$$\mathbf{J}_\gamma^i = -\phi\rho_\gamma S_\gamma \frac{M^i}{M_\gamma}\left(\tau_\gamma D_\gamma^i\right)\nabla\chi_\gamma^i \quad (3)$$

where M (kg/kmol) is molecular weight, τ (−) tortuosity, D (m^2/s) diffusion coefficient and χ (−) mole fraction.

Simulations were performed using Subsurface Transport Over Multiple Phases (STOMP), an open source software package developed by the Pacific Northwest National Laboratory's Hydrology Group [17]. The STOMP simulator solves the partial-differential equations that describe the

Table 1 Fluid properties at room conditions (T = 22 °C, P = 101,325 Pa)

	Pure water	Water saturated in dissolved CO_2	Variations (%)
Dissolved CO_2 mass fraction at saturation	_	1.53×10^{-3}	_
Water viscosity (Pa s)	9.5475×10^{-4}	9.5225×10^{-4}	0.26 (decrease[a])
Water density (kg/m^3)	997.95	998.24	0.029 (increase[a])
Diffusion coefficient of dissolved CO_2 in pure water (m^2/s)	1.4424×10^{-9}	1.4481×10^{-9}	0.4 (increase[a])

[a] Increase means that the property of pure water is lower than the one of water saturated by dissolved CO_2

conservation of mass quantities by using integrated-volume finite-difference discretization to the physical domain and backward Euler discretization to the time domain. Since the resulting equations are nonlinear coupled algebraic equations, the Newton–Raphson iteration method is used to solve them. STOMP has numerous operational modes allowing the user to choose the governing equations that are to be solved, with the related constitutive equations. For the present work, STOMP Operational mode STOMP-WCS (Water–CO_2–Salt) was used even though simulations are run for CO_2 in water only with no brine.

3.2.2 State equations

A detailed description of all the state equations used in STOMP-WCS can be found in [17]. The phase equilibrium is computed following the H_2O and CO_2 mutual solubility calculation method developed by Spycher et al. [18]. Aqueous density and viscosity are calculated under equilibrium conditions depending on the temperature and pressure conditions, the CO_2 properties and the dissolved CO_2 mass fraction following Alendal and Drange [19] and Kumagai and Yokoyama [20]. The aqueous molecular diffusion is computed as a function of aqueous viscosity and CO_2 gas viscosity using the formulation of Renner [21] and so depends on the dissolved CO_2 mass fraction. In our configuration, the differences between the fluid properties of pure water and water containing dissolved CO_2 at saturation value remained low (Table 1). In particular, the convection phenomenon was driven by a density increase of about 0.03 %.

3.2.3 Saturation and relative permeability

The porous medium representing the Hele-Shaw cell in our numerical simulations was assumed to have a porosity equal to unity, an intrinsic permeability related to the cell gap by $k = b^2/12$ and a saturation function maximizing the sharpness of the interface between the liquid and gas phases.

Typical saturation functions (capillary-pressure curves) may be represented by the Brooks-Corey (BC) model or the Van Genuchten (VG) one. Li et al. [22] studied the influence of this representation on the CO_2 dissolution and density driven convection processes. They found that the VG model enhanced the CO_2 dissolution compare to the BC-type representation. Therefore, to optimize the phase contact and maximize the sharpness of the interface between the liquid and gas phases, we used a Van Genuchten saturation function (Eq. 4) with very high parameter values ($\alpha = 1{,}000$; $n = 7$). With these model and parameters, we obtained aqueous saturations varying from 1 to 10^{-3} in less than 1 mm across the liquid/gas interface.

$$S_{el} = \frac{S_l - S_r}{1 - S_r} = \left[1 + (\alpha h_c)^n\right]^{-m} \tag{4}$$

S_{el} and S_r are the effective and irreducible water saturations; α (1/m), n (−) and $m = 1 - 1/n$ are the Van Genuchten parameters and $h_c = h_g - h_l$ (m) is the pressure head difference between phases.

The saturation function was associated with two Mualem relative permeabilities functions for the gas and aqueous solutions (Eq. 5). The Mualem functions are effective in enforcing sharp contrast in transport properties across the gas–liquid interface.

$$k_{rl} = (S_{el})^{1/2}\left[1 - \left(1 - (S_{el})^{1/m}\right)^m\right]^2 \text{ and } k_{rg} = (1 - S_{el})^{1/2}\left[1 - \left(1 - (S_{el})^{1/m}\right)^m\right]^2 \tag{5}$$

3.2.4 Boundaries and initial conditions

Boundary and initial conditions simulated the experimental ones. The flow domain was initially at hydrostatic pressure gradient. Temperature of the room was assumed to be constant at 22 °C. The top boundary was at atmospheric pressure conditions. No flow conditions were imposed for the bottom and lateral boundaries. The boundary condition equations are summarized in Table 2.

For the single-phase simulations, we imposed a saturation condition in dissolved CO_2 at the upper boundary as STOMP-WCS computes automatically the corresponding constant concentration which may change depending on temperature and pressure. For the multiphase simulations a 3 cm-high layer of CO_2 gas was overlaying the aqueous-saturated part of the domain and the gas pressure was

Table 2 Boundary condition equations

Boundary	Concentration	Velocity	Pressure
Top			
Single phase	$C_l^{CO_2} = saturation$	–	$P_l = P_{atm}$
Multiphase	Pure CO_2 gas	–	$P_g = P_{atm}$
Bottom	$\frac{dC_l^{CO_2}}{dz} = 0$	$\frac{dV_l}{dz} = 0$	–
Left	$\frac{dC_l^{CO_2}}{dx} = 0$	$\frac{dV_l}{dx} = 0$	–
Right	$\frac{dC_l^{CO_2}}{dx} = 0$	$\frac{dV_l}{dx} = 0$	–

considered equal to atmospheric pressure at the top. Figure 1a, b show both configurations.

In order to induce convection in a homogeneous medium, small fluctuations must be added to the initial conditions. Some authors [12] used numerical rounding errors to trigger the instabilities while others included small sinusoidal perturbations in the initial condition (at time t = 0). Following Farajzadeh et al. [14], we used small sinusoidal perturbations to induce convection. For the single phase configuration, the perturbations were superimposed to the top boundary condition. For the multiphase simulation, the perturbations were located just below the interface with the gas phase.

3.2.5 Taylor dispersion

In a porous medium, hydrodynamic dispersion of solutes results from the combination of molecular diffusion and pore velocity variations (mechanical dispersion). Hidalgo and Carrera [12] concluded that mechanical dispersion had a significant effect on the onset time of convection during CO_2 sequestration but did not study long-term results. In a Hele-Shaw cell such as the one used here, the mechanical dispersion is reduced to Taylor dispersion, which results from Poiseuille-type velocity variations across the cell aperture. Taylor dispersion in fractures or micro-channels was shown to have an important effect on transport of solutes in an experimental configuration similar to ours, even in cases of low flow velocities [23–25].

The Taylor dispersion coefficient for dissolved CO_2 in the parallel-plate aperture is [23]:

$$D_{Tay} = \frac{U^2 b^2}{210 D_l^{CO_2}} \tag{6}$$

where U is the average velocity in the flow direction and $D_l^{CO_2}$ is the molecular diffusion of dissolved CO_2 in water. Table 3 shows D_{Tay} values calculated using average velocities estimated experimentally from the time of first arrival of dissolved CO_2 at the cell bottom.

As seen it Table 3, Taylor dispersion increases the hydrodynamic dispersion coefficient by a factor of 2 to 5. Accordingly, the diffusion coefficient $D_l^{CO_2}$ in Eq. 3 was replaced by $D_l^{CO_2} + \frac{U^2 b^2}{210 D_l^{CO_2}}$ in order to take the Taylor dispersion effect into account.

3.2.6 Permeability fields

Since the permeability is proportional to the square of the cell aperture, a small variation in aperture will result in a significant variation in permeability affecting the flow phenomenon. As direct measurements of the Hele-Shaw aperture on the top of the cell showed significant variations for the two cells of Table 3, discrepancies between experimental and numerical results were expected if the permeability field is considered as uniform in the simulations.

At first, we used the direct measure of the aperture variations on the top of the cell to build permeability fields varying linearly in the horizontal direction but assuming no aperture variation in the vertical direction (Fig. 2a). To improve the agreement between the physical model used in numerical simulation and the experiments, we applied the methodology developed by Detwiler et al. [26] to measure the aperture variations in the whole Hele-Shaw cell [27]. The measurements were used to calculate numerical non-uniform permeability fields representative of the aperture variation in the experimental Hele-Shaw cells (Fig. 2b). Figure 2a, b are representatives of the permeability fields obtained with b = 1 mm, where the lighter regions indicate higher permeability.

3.2.7 Initial numerical considerations

Meshes were refined at the locations where the convection fingering process initiates (on the top for the single phase simulation and at the interface between gas and water for the two-phase simulation). The vertical spacing varied from 0.05 mm at the top to 3 mm at the bottom of the cell. Space discretization near the top (or the gas/water interface) should effectively be smaller than the expected diffusive layer thickness. According to Pruess [10] the diffusive layer

Table 3 Taylor dispersion coefficient calculated from experimental average velocity

	U (m/s)	D_{Tay} (m^2/s)	$D_{hydr} = D_l^{CO_2}$ (m^2/s)	$D_{hydr} = D_{Tay} + D_l^{CO_2}$ (m^2/s)
b = 1 mm	4.418×10^{-5}	6.44×10^{-9}	1.44×10^{-9}	7.88×10^{-9}
b = 0.7 mm	3.245×10^{-5}	1.703×10^{-9}	1.44×10^{-9}	3.143×10^{-9}

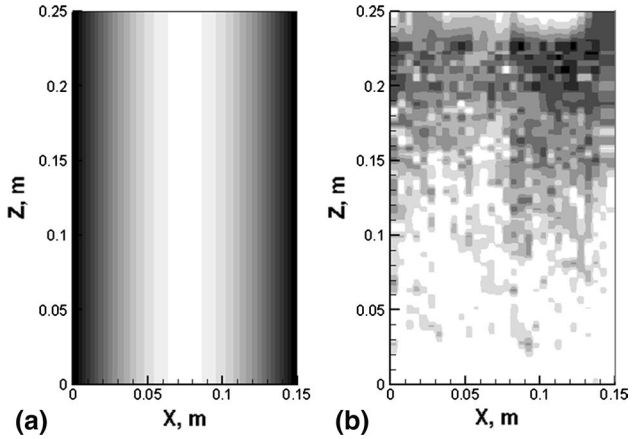

Fig. 2 Permeability fields resulting from **a** the direct aperture measurements at the top of the cell and **b** the transmitted light analysis for b = 1 mm

thickness h can be calculated using the molecular diffusion coefficient $D_l^{CO_2}$ and the onset time of convection t_{conv}:

$$h = \sqrt{D_l^{CO_2} t_{conv}} \tag{7}$$

According to the experimental results convection was not active during the first minute [4]. Therefore a vertical grid dimension equal to 0.05 mm near the top (corresponding to an onset time of less than 2 s) was considered appropriate. The horizontal grid spacing was assumed uniform and had to remain inferior to the expected thickness of the convection fingers [10]. Since evaluation of the finger thickness is difficult, different values from 5 to 0.5 mm were tested. In all the computations, the Newton–Raphson convergence criterion was chosen to be 1×10^{-6} in order to ensure sufficient accuracy without overly increasing the computational time [17].

The effect of the perturbations as an initial condition may also be questioning. Farajzadeh et al. [13] asserted that the long term behavior does not depend on the initial perturbation. They observed in their simulations that after some time the number of fingers is less than the number of periods in the initial perturbation. Looking at the experimental onset of convection patterns [4], we noticed that the phenomenon starts with numerous fingers (more than 30 fingers whatever the Hele-Shaw cell). Considering this experimental feature, we triggered the convection phenomenon using at least 30-waves perturbations and noticed that the fingering evolution is independent of the perturbation wavelength. We also analyzed the impact of the amplitude perturbation on the mass transfer phenomenon. At small magnitudes (10^{-4}–10^{-6}), we did not notice any significant changes on the dissolved CO_2 mass transfer (mass variations remain less than a few %) but only on the onset time of convection.

4 Results and discussion

4.1 Numerical considerations on dissolved CO_2 mass flux

4.1.1 Single phase simulations

The mesh refinement is assumed to lead to an accurate resolution when the mass flux of dissolved CO_2 does not vary significantly anymore with mesh changes. A mesh sensitivity study was carried out and we concluded that the grid resolution was adequate when the CO_2 mass transfer remained stable. In Table 4, we present results of total mass of dissolved CO_2 for four different meshes. Total dissolved CO_2 mass results are reported for comparison when dissolved CO_2 reaches the bottom of the cell. In terms of mass transfer, the mesh of 150 columns (grid length of 1 mm) by 173 rows (mesh refined down to 0.05 mm) was optimal since no significant differences were obtained with a greater mesh refinement. Note that the simulation using a mesh of lower resolution (150 columns by 128 rows) resulted in an overestimation of the mass transfer. In Table 5, we also show the effect of a decrease in the Newton–Raphson convergence criterion value on the total mass of dissolved CO_2 result. No significant differences in the results were found proving the relevance of the 1×10^{-6} Newton–Raphson criterion to control time steps.

4.1.2 Two-phase simulations

For the two-phase simulation, the mesh was built such that the gas/water interface (where CO_2 dissolution occurs) as well as the higher part of the water-saturated cell (where convection initiates) was included in the most refined grid part (0.05 mm). The resulting mesh (including the gas layer) was composed of 150 columns by 212 rows. We led some tests to refine the zone of CO_2 dissolution/convection

Table 4 Numerical total mass of dissolved CO_2 at the first arrival time of CO_2 at the bottom obtained using four different meshes (single-phase simulations)

Mesh (columns × rows)	150 × 128	150 × 173	300 × 192	300 × 256
Total dissolved CO_2 mass (kg) at the first arrival time of CO_2 at the bottom	1.78×10^{-5}	1.69×10^{-5}	1.69×10^{-5}	1.69×10^{-5}

Table 5 Numerical total mass of dissolved CO_2 at the first arrival time of CO_2 at the bottom obtained using four different values of the Newton–Raphson criterion (single-phase simulations, mesh of 150 columns by 173 rows)

Newton–Raphson convergence criteria	10^{-5}	10^{-6}	10^{-8}	10^{-10}
Total mass of dissolved CO_2 (kg) at the first arrival time of CO_2 at the bottom	1.8×10^{-5}	1.690×10^{-5}	1.704×10^{-5}	1.695×10^{-5}

initiation (refinement to 0.025 mm) without noticing any significant change in the total CO_2 mass transfer.

Therefore, total dissolved CO_2 mass computations confirm the suitability of using the 150 × 173 mesh (150 × 212 mesh for two phases) for an accurate simulation of the density driven convection phenomenon.

4.2 Single and two-phase simulations (constant aperture)

4.2.1 Single phase simulations

As initial conditions for the single phase simulations, we used a small sinusoidal perturbation in dissolved CO_2 saturation at the top boundary with a slightly larger wave length in the center. We checked firstly that this numerical procedure did not affect the mass transfer and the timescale significantly, however it allowed inducing convection preferentially in the central part of the cell (instead of preferential flow on the sides), similar to what was observed during the experiments. This preferential fingering in experiments was attributed to a central location of the CO_2 injection on the top of the cell and a bigger aperture in the central part of the cell [4]. Note that (except for b = 0.3 mm) the central single-finger pattern induced by the initial perturbations does not persist as convection develops (Fig. 3, column 2).

From Tables 6 and 7 we can compare the single phase numerical simulations and the experimental results in terms of first arrival time of dissolved CO_2 at the bottom of the cell and the total dissolved CO_2 mass. As the total dissolved CO_2 mass was determined experimentally only for the 1 mm- and 0.7 mm-gap Hele-Shaw cell configurations [27], we can just compare the numerical mass transfer results with the experimental values for these two configurations. For the two other experimental configurations (b = 0.5 mm and b = 0.3 mm), only the timescale and convection patterns are available for comparison.

For the 1 and 0.7 mm-gap cells, the first arrival time of dissolved CO_2 at the bottom of the cell was smaller in the one-phase numerical simulations than in the experiments (Table 6). Moreover the total CO_2 mass was considerably overestimated (Table 7). This result is not surprising because the boundary condition of constant saturation in dissolved CO_2 at the top of the cell implies a constant flux of dissolved CO_2 into the convective fingers. Figure 3 compares the experimental convection patterns (column 1) obtained for the four cells and the corresponding one-phase numerical results (column 2) before the arrival of dissolved CO_2 at the bottom of the cell. We can notice some similarities between numerical and experimental results looking at the main fingers. In particular, a greater number of fingers are observed in the cell with the 1 mm-aperture than the thinner one. However one-phase numerical simulations failed to generate the same number of fingers than the experiments: in particular the small fingers near the top interface as observed in experimental snapshots are missing. These results suggest that neither the characteristic timescale of convection nor the total mass transfer of dissolved CO_2 can be adequately estimated using a boundary condition of fixed dissolved CO_2.

4.2.2 Two-phase simulations

Comparing the two phase numerical simulation results and their corresponding experimental results (Table 5), we found similarly to Kneafsey and Pruess [2] that taking into account the dissolution process at the gas/water interface leads to an overestimation of the computed timescale compared to the experimental one. CO_2 mass transfer is also numerically overestimated but the differences with the experimental results are lower than the ones obtained with single phase simulations (Table 6).

Comparing the convection patterns (Fig. 3), the two phase simulations (column 3) succeed in reproducing the generation of small fingers at the top of the cell, which single phase simulations failed to predict (column 2). Also the total number of fingers is in better agreement with experiments whatever the configuration.

4.2.3 Comparison of single phase and two-phase simulations

Figure 4 compares the flux of dissolved CO_2 entering the cell depending on the top boundary condition. The Fick's law solution is used as a reference curve. In single phase simulation, assuming fixed dissolved CO_2 concentration at the top boundary leads to a perfect fit of the numerical flux curve with the corresponding analytical Fick's law solution at early times. After about 40 s for the 1 mm aperture cell, convection begins and the flux of dissolved CO_2 entering the cell increases sharply.

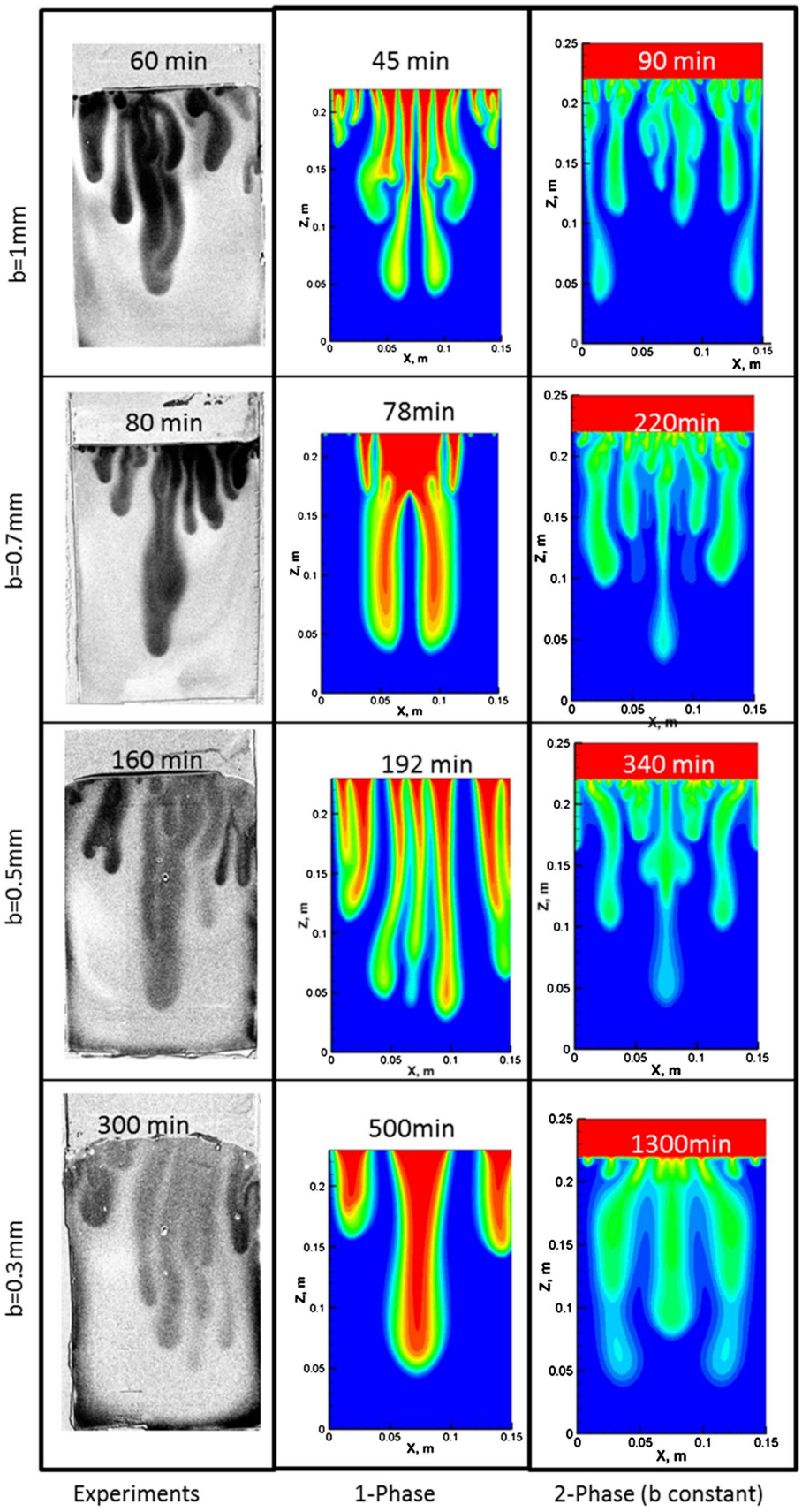

Fig. 3 Experimental and numerical convection patterns (aqueous CO_2 concentration) for the four Hele-Shaw configurations with constant aperture (*first column* experimental snapshots, *second column* single phase simulation, *third column* two-phase simulation). *Each row* displays results for a different aperture value (*first row* b = 1 mm, *second row* b = 0.7 mm, *third row* b = 0.5 mm and *last row* b = 0.3 mm)

Table 6 Experimental and numerical first arrival time of dissolved CO_2 to the bottom of the cell for the 4 configurations of Hele-Shaw cell and the different numerical assumptions

b (mm)	Experiments	One phase simulations	Two-phase simulations			
			Constant permeability	Constant permeability with Taylor dispersion	Linearly varying permeability	Heterogeneous permeability field
1	83	54	102	111	78	99
0.7	113	96	245	246	228	135
0.5	183	210	436			
0.3	412	500	1,700			

Table 7 Experimental and numerical dissolved CO_2 mass at the first arrival time of dissolved CO_2 to the bottom of the cell for the four configurations of Hele-Shaw cell and the different numerical assumptions

b (mm)	Experiments	One phase simulations	Two-phase simulations			
			Constant permeability	Constant permeability with Taylor dispersion	Linearly varying permeability	Heterogeneous permeability field
1	5.00E−06	1.65E−05	7.66E−06	8.02E−06	6.41E−06	6.69E−06
0.7	3.00E−06	1.44E−05	5.80E−06	5.84E−06	6.90E−06	4.28E−06
0.5		7.93E−06	4.03E−06			
0.3		5.11E−06	3.43E−06			

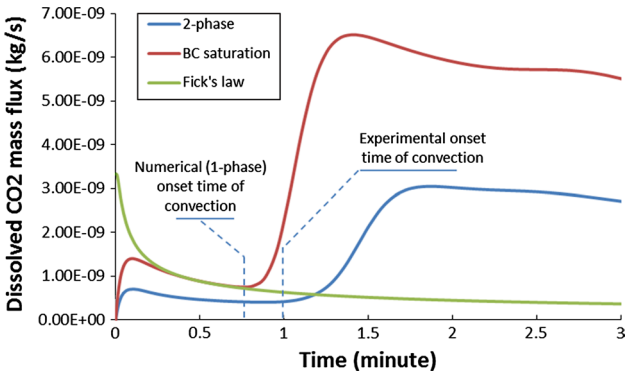

Fig. 4 Dissolved CO_2 mass flux at the top of the cell for the two simulations (one phase and two-phase) during the first 3 min (b = 1 mm)

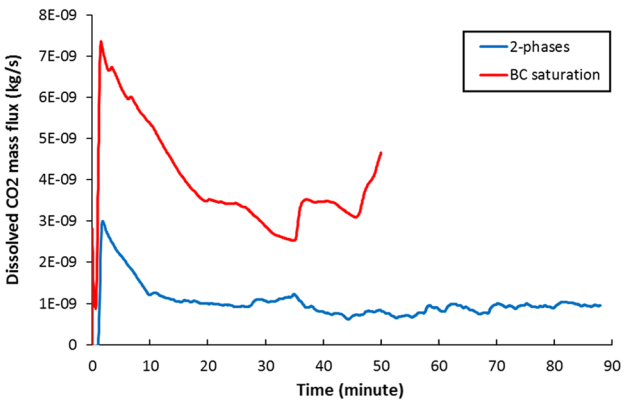

Fig. 5 Dissolved CO_2 mass flux at the top of the cell for the two simulations (one phase and two-phase) from t = 0 to the first arrival time of dissolved CO_2 at bottom (b = 1 mm)

In two-phase simulations, the numerical flux curve of dissolved CO_2 does not coincide anymore with the analytical Fick's law solution. This result was expected as Fick's law assumes a boundary condition of constant concentration for the diffusive transfer. In two-phase simulation, the dissolution process of CO_2 through the water/gas interface is considered, leading to lower values of dissolved CO_2 concentration on the top of the water-saturated part of the cell. The onset of convection starts later than that obtained in single phase simulation and is in better agreement with the experimental one (Fig. 4). The convection rate is slower, resulting in a lower flux of dissolved CO_2 by a factor of about 3.

Looking at the temporal evolution (Fig. 5), we can notice that the dissolved CO_2 mass flux curves have the same feature for both boundary conditions. The dissolved CO_2 mass flux increased sharply while convection begins. After about 2 min, the mass flux rates start to decrease reaching a more or less constant value after 15–20 min. However, along the whole process, the dissolved CO_2 mass flux remains three times lower with the gas phase boundary than with the fixed concentration boundary. The flux induced by convection is also more stable when the presence of the gas phase is considered.

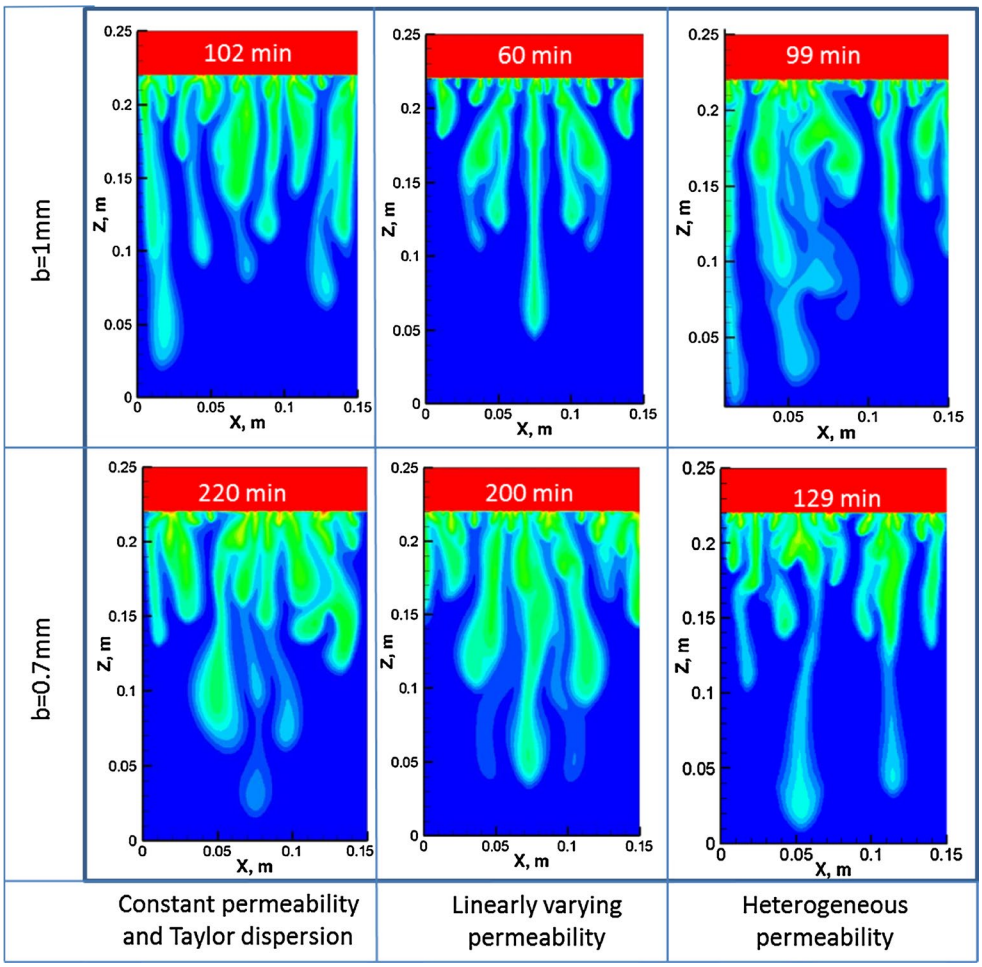

Fig. 6 Experimental and numerical convection patterns (aqueous CO_2 concentration) for the four Hele-Shaw configurations with constant aperture (*first column* experimental snapshots, *second column* single phase simulation, *third column* two-phase simulation). *Each row* displays results for a different aperture value (*first row* b = 1 mm and *second row* b = 0.7 mm)

The difference between single and two-phase simulations can be reduced if the thickness of the transition zone in the two-phase simulations is increased (decrease in the Van Genuchten parameter values). A thick transition zone means a bigger gas/water mixing zone above the saturated part of the medium. This condition tends to be similar to a boundary condition of saturation in dissolved CO_2 but is far from the experimental conditions related to a Hele-Shaw cell.

4.3 Two-phase simulations with Taylor dispersion effect

Comparing the two-phase with constant permeability simulation results without Taylor dispersion (Fig. 3, column 3) and with Taylor dispersion (Fig. 6, column 1), we observed that Taylor dispersion did not induce noticeable changes in the simulation results, neither for the pattern results, nor for the timescale. Dispersion only seemed to slow down convection slightly. This trend was expected as the dispersion phenomenon tends to diminish the amplitude of the concentration gradients in the cell. Patterns were also found to be less symmetrical. In terms of total dissolved CO_2 mass, the results with and without dispersion were quite similar (Table 6). In this particular condition of Hele-Shaw cell with no forced flow, the mechanical dispersion did not significantly affect the convection propagation.

4.4 Two-phase simulations (b variable)

4.4.1 Linearly varying permeability fields

Taking into account the aperture variations at the top, the agreement between the experimental and numerical timescale and dissolved CO_2 mass results was better, in the case of the b = 1 mm cell (Tables 5, 6). However, numerical results were not improved compare to experimental ones for the b = 0.7 mm. So it appears clearly that variations in the aperture played a significant role in the convection propagation in the experiments but was not correctly taken into account by using measurement at the top of the cells.

4.4.2 Heterogeneous permeability fields

Variations of the cell aperture may explain experimental observations such as preferential fingering phenomenon in the

central part of the cell, and reduced experimental timescales and total CO_2 masses compared to numerical simulations. We, therefore, performed simulations using the heterogeneous permeability fields (Fig. 2) determined using the transmitted light analysis method developed by Detwiler et al. [26].

Comparing the experimental results and the two phase simulation results with the heterogeneous permeability fields, we found that although both arrival time and total mass of dissolved CO_2 are still overestimated, incorporating aperture variations significantly improve the agreement with the experimental observations (Tables 6, 7). We also obtained improved simulations of the fingering morphology as they are in better agreement with the experimental fingering morphology (compare Figs. 3, column 1, 6, column 3). For both cells the experimental convection patterns were asymmetrical, a feature well reproduced numerically when measured aperture variations are included in the simulations.

5 Conclusions

Single phase and two-phase numerical modeling of density driven convection of dissolved CO_2 in a water saturated Hele-Shaw cell was presented. Simulations were validated by corresponding experimental results. The presence of the gas phase as well as the experimental cell aperture variations were very important for obtaining accurate simulation of the CO_2 mass transfer timescale and amplitude. On the other hand, Taylor dispersion was found to have very limited effect on the overall density driven convection phenomenon.

Acknowledgments We would like to acknowledge Masdar Institute for the financial support of this collaboration project with MIT, Dr. Mark White from Pacific Northwest National Laboratory for his help with the STOMP simulator as well as Dr. Mohamed Mekias for his support in computational issues.

References

1. Ennis-King J, Paterson L (2005) Role of convective mixing in the long-term storage of carbon dioxide in deep saline formations. Soc Petrol Eng J 10:349–356
2. Kneafsey TJ, Pruess K (2010) Laboratory flow experiments for visualizing carbon dioxide-induced density-driven brine convection. Transp Porous Med 82:123–139
3. Kneafsey TJ, Pruess K (2011) Laboratory experiments and numerical simulation studies of convectively enhanced carbon dioxide dissolution. In: Proceedings of the GHGT-10 conference, energy procedia 4:5114–5121
4. Faisal TF, Chevalier S Sassi M (2013) Experimental and Numerical studies of density driven natural convection in saturated porous media with application to CO_2 geological storage. In: Proceedings of the GHGT-11 conference, energy procedia 37:5323–5330
5. Xu X, Chen S, Zhang D (2006) Convective stability analysis of the long-term storage of carbon dioxide in deep saline aquifers. Adv Water Resour 29:397–407
6. Riaz A, Hesse M, Tchelepi HA, Orr FM (2006) Onset of convection in a gravitationally unstable diffusive boundary layer in porous media. J Fluid Mech 548:87–111
7. Javaheri M, Abedi J, Hassanzadeh H (2010) Linear stability analysis of double-diffusive convection in porous media with application to geological storage of CO_2. Transp Porous Med 84:441–456
8. Pau GSH, Bell JB, Pruess K, Almgren AS, Lijewski MJ, Zhang K (2010) High-resolution simulation and characterization of density-driven flow in CO_2 storage in saline aquifers. Adv Water Resour 33:443–455
9. Slim AC, Ramakrishnan TS (2010) Onset and cessation of time-dependent dissolution-driven convection in porous media. Phys Fluids 22:124103
10. Pruess K (2008) Numerical modeling studies of the dissolution-diffusion-convection process during CO_2 storage in saline aquifers, Lawrence Berkeley National Laboratory. http://www.escholarship.org/uc/item/2fc5v69p. Accessed 6 April 2014
11. Battistelli A, Claudio C, Pruess K (1997) The simulator TOUGH2/EWASG for modelling geothermal reservoirs with brines and noncondensible gas. Geothermics 26:437–464
12. Hidalgo JJ, Carrera J (2009) Effect of dispersion on the onset of convection during CO_2 sequestration. J Fluid Mech 640:441–452
13. Farajzadeh R, Salimi H, Zitha PLJ, Bruining H (2007) Numerical simulation of density-driven natural convection in porous media with application for CO_2 injection projects. Int J Heat Mass Transf 50:5054–5064
14. Farajzadeh R, Ranganathan P, Zitha PLJ, Bruining J (2011) The effect of heterogeneity on the character of density-driven natural convection of CO_2 overlying a brine layer. Adv Water Resour 34:327–339
15. Ranganathan P, Farajzadeh R, Bruining H, Zitha PLJ (2012) Numerical simulation of natural convection in heterogeneous porous media for CO_2 geological storage. Transp Porous Med 95:25–54
16. Farajzadeh R, Zitha PLJ, Bruining H (2009) Enhanced mass transfer of CO_2 into water: experiment and modeling. Ind Eng Chem Res 48:6423–6431
17. White MD, Watson DJ, DH Bacon, White SK, McGrail BP, Zhang ZF (2012) STOMP, subsurface transport over multiple phases, STOMP-CO2 and -CO2e Guide, PNNL-21268, U.S. department of ENERGY, pp 270
18. Spycher N, Pruess K, Ennis-King J (2003) CO_2–H2O mixtures in geological sequestration of CO2. I. Assessment and calculation of mutual solubilities from 12 to 100 C and up to 600 bar. Geochim Cosmoschim Acta 67:3015–3031
19. Alendal G, Drange H (2011) Two-phase near-field modeling of purposefully released CO_2 in the ocean. J Geophys Res 106(C1):1085–1096
20. Kumagai A, Yokoyama C (1999) Viscosities of aqueous NaCl solutions containing CO_2 at high pressures. J Chem Eng Data 44:227–229
21. Renner TA (1988) Measurement and correlation of diffusion coefficients for CO_2 and rich-gas applications. SPE Reserv Eng 3:517–523
22. Li B, Tchelepi HA, Benson SM (2013) The influence of Capillary entry-pressure representation on CO2 solubility trapping. In: Proceedings of the GHGT-11 conference, energy procedia 37:3808–3815
23. Detwiler RL, Rajaram H, Glass RJ (2000) Solute transport in variable-aperture fractures: an investigation of the relative

importance of Taylor dispersion and macrodispersion. Water Resour Res 36:1611–1625
24. Boschan A, Charette VJ, Gabbanelli S, Ippolito I, Chertcoff R (2003) Tracer dispersion of non-Newtonian fluids in a Hele-Shaw cell. Phys A 327:49–53
25. Bontoux N, Pepin A, Chen Y, Ajdari A, Stone HA (2006) Experimental characterization of hydrodynamic dispersion in shallow microchannels. Lab Chip J 6:930–935
26. Detwiler RL, Pringle SE, Glass RJ (1999) Measurement of fracture aperture fields using transmitted light: an evaluation of measurement errors and their influence on simulations of flow and transport through a single fracture. Water Resour Res 35:2605–2617
27. Faisal TF, Chevalier S, Bernabe Y, Juanes R, Sassi M (2015) Quantitative and qualitative study of density driven CO_2 mass transfer in a vertical Hele-Shaw cell. Int J Heat Mass Transf 81:901–914